



OPEN

Integration of plasmonic AgPd alloy nanoparticles with single-layer graphitic carbon nitride as Mott-Schottky junction toward photo-promoted H₂ evolution

Behnam Gholipour¹, Afsaneh Zonouzi^{1✉}, Mohammadreza Shokouhimehr³ & Sadeqh Rostamnia^{2✉}

Plasmonic AgPd alloy nanoparticles (AgPd_{NPs}) decorated on single-layer carbon nitride (AgPd_{NPs}/SLCN) for the designing of the Mott-Schottky junction were constructed with the ultrasonically assisted hydrothermal method and used toward photo evolution H₂ from formic acid (FA) at near room temperature (30 °C). The Pd atom contains active sites that are synergistically boosted by the localized surface plasmon resonance (LSPR) effect of Ag atoms, leading to considerably enhanced photocatalytic properties. The photoactive AgPd_{NPs}/SLCN obtained supreme catalytic activity to produce 50 mL of gas (H₂ + CO₂) with the initial turnover frequency of 224 h⁻¹ under light irradiation. The catalyst showed stable catalytic performance during successive cycles.

Access to alternative and clean energy sources has become one of the most important issues due to the increasing demand for energy and the reduction of the use of conventional fossil fuels^{1–3}. Due to the exhaustion of fossil fuels and ecological issues, hydrogen-based fuel is one of the most hopeful clean and sustainable energy sources for current society^{4–8}. Currently, the industrial method for the production of hydrogen is mainly done through vapor reforming and coal gasification, which is based on confined fossil sources such as natural gas, coal, and oil. Based on mid to long-term plans, there is a growing requirement for substitute feedstocks for the production of H₂ in a more sustainable way^{9,10}. In recent years, various chemical hydrogen storing materials, such as methanol, formic acid, formaldehyde and boron ammonia have been extensively studied^{11–22}. Formic acid (FA) as a hopeful material in H₂ production/storage has engrossed much consideration owing to its great gravimetric/volumetric H₂ capacity, easiness of use, non-toxicity, ambient temperature stability and plentiful supply from the transformation of biomass and carbon dioxide^{23–28}.

For the use of FA as a liquid organic H₂ carrier (LOHC), the expansion of competent catalysts, especially heterogeneous catalysts for FA decomposition, is a challenging issue^{29,30}. On the other hand, over the past decades, the field of heterogeneous photocatalysis has extended swiftly and has faced various developments, particularly in regard to energy and the environment. Accordingly, in recent years, photocatalytic degradation of FA to CO₂ and H₂ has been broadly studied in the literature^{31–35}. Recent reports have shown that the design and manufacture of conjugated semiconductor polymers due to their advantages such as constancy in aqueous-medium, visible light absorbency, intramolecular charge transition, the low expense is one of the effective strategies^{36–38}. Supported semiconductors with visible light absorption can be used to modify the photocatalytic operation of heterogeneous metal based catalysts for photo-decomposition formic acid^{31,32,35,39,40}. This is owing to the electronic interaction and electron handover between the metal and the semiconductor due to the Mott-Schottky effect on the surface of the metal based semiconductor interfaces⁴¹. The integration of plasmonic based alloy

¹Department of Chemistry, University of Tehran, P.O. Box 14155-6455, Tehran, Iran. ²Organic and Nano Group (ONG), Department of Chemistry, Iran University of Science and Technology (IUST), PO Box 16846-13114, Tehran, Iran. ³Department of Materials Science and Engineering, Research Institute of Advanced Materials, Seoul National University, Seoul 08826, Republic of Korea. ✉email: zonouziafsaneh@ut.ac.ir; rostamnia@iust.ac.ir

(AgPd and AuPd) and semiconductors to make Mott-Schottky photocatalysts is an effective manner to improve photocatalytic operation by accelerating the charge kinetics of photocatalytic reactions^{32,35,42}.

Carbon nitride (g-C₃N₄) has been widely used as one of the most important photocatalyst in the production of hydrogen by visible light^{43–46}. This is due to the π -conjugated graphitic carbon nitride structure that provides a specific electronic property for charge transfer^{47–50}. On the other hand, as an active semiconductor in visible light, it has a relatively narrow bandgap of 2.7 eV and favorable conduction band (C_b) and valence band (V_b), which is appropriate for UV–vis light absorption for hydrogen evolution^{47,51–59}. The most important point is that the performance of most noble metals is betwixt the C_b and the V_b of graphitic carbon nitride, which leads to the high reinforcement of the handover of photogenerated electrons from graphitic carbon nitride to metal nanoparticles owing to the Mott-Schottky effect^{32,35}. In 2017, Wu et al. reported the monodisperse of AgPd alloy on graphite carbon nitride semiconductor (AgPd/CN) for photocatalytic evolution of hydrogen from formic acid³¹. Yu et al. offered the Mott-Schottky heterojunction based on AgPd NWs and g-C₃N₄ for photocatalytic dehydrogenation of FA in the presence of visible light ($\lambda > 400$ nm)³⁵. Recently, Cheng et al. reported graphite carbon nitride nanosheet containing AgPd bimetallic nanoparticles with Ag plasmonic effect as an effective Mott-Schottky photocatalyst to catalyzing the evolution of H₂ from the formic acid under visible light⁴². Compared to bulk g-C₃N₄, the single layer carbon nitride is an emerging photocatalyst with a layered structure due to its unique properties such as photogenerated charge carrier lifetime, specific surface area, shorter bulk diffusion length, and high carrier density reduces the possibility of recombination of charge carriers and affords more surface-active sites for metal stabilization^{60–63}. Inspired by the aforesaid considerations and in line with our recent efforts in the field of clean energy and hydrogen production^{28,64–69}, here we offer the synthesis of bimetallic AgPd_{NPs} decorated on single layer carbon nitride (SLCN) as an active plasmonic photocatalyst for the evolution of H₂ from FA.

Experimental

Materials and methods. Melamine (Aldrich, 99%), AgNO₃ (Aldrich, 99.99%), K₂PdCl₄ (Aldrich, 99.9%), Formic acid (Merck, 98–100%), KCl (Merck, 99.99%), NaBH₄ (Merck, 99%) were used without additional refinement. Ultrapure water (18.5 M Ω Milli Q) was utilized for all experimentations.

Characterization. FT-IR spectrums were recorded by a Shimadzu IR-460 spectrometer. Powder X-ray diffraction (PXRD) patterns were performed for samples using the D₈ ADVANCE X-ray diffractometer diffraction system with Cu K α radiation ($\lambda = 1.5406$ Å). UV–vis absorption and diffuse reflectance spectra were recorded using SHIMADZU, UV -2450. The surface morphology of samples was determined by the Hitachi S4700 FE-SEM. TEM images were captured with a Zeiss EM 900 electron microscope. The generated gas molecules (H₂ + CO₂) were monitored by gas chromatography (GC) armed with a TCD detector and the results were contrasted with the automatic CO₂ gas measuring apparatus.

Synthesis of g-C₃N₄. Synthesis of g-C₃N₄ using thermal polymerization of melamine was carried out in an alumina crucible with a cover, from ambient temperature up to 550 °C at a heating rate of 2.3 °C per minute under air conditions in a muffle furnace. In the following, by keeping the temperature constant at 550 °C for 4 h the yellow g-C₃N₄ was obtained⁷⁰.

Synthesis of SLCN. Synthesis of g-C₃N₄ was executed using a complementary two-step manner (ultrasonic-hydrothermal method). For this purpose, 0.1 g of as-made bulk g-C₃N₄ was first exposed to ultrasonic waves for 2 h. In the following, after resting the obtained solution for 5 min, the upper part of the solution was separated and rendered into a Teflon-lined stainless autoclave (100 ml) and then heated at 120 °C for 10 h. Eventually, after the desired time had elapsed and the autoclave temperature reached ambient temperature, the almost yellowish white mixture was isolated by centrifugation (5000 rpm) and dried up at 50 °C for 12 h.

Synthesis of AgPd_{NPs}/SLCN. For the synthesis of AgPd_{NPs}/SLCN, 0.1 g SLCN was dispersed in 40 mL distilled water and then sonicated at 25 °C for 30 min. Subsequently aqueous AgNO₃ and K₂PdCl₄ (mole ratio = 1:0, 2:1, 1:1, 1:2, 0:1) was extra, and then magnetically stirred for overnight at ambient temperature. Afterward, 2.5 mL of aqueous NaBH₄ (0.15 M) was added drop by drop into the mixture and stirred for another 2 h. After 2 h, the samples were gathered by centrifugation (5000 rpm) and rinsed with distilled water several times. The samples were dried in an oven at 50 °C for 15 h.

Photocatalytic dehydrogenation of FA. The photocatalytic H₂ evolution assessment was performed in a closed 50 mL reactor by a 24 W LED-SMD lamp. For this purpose, in 10 ml of deionized water, 20 mg of AgPd_{NPs}/SLCN catalyst was dispersed by sonication and the reactor oxygen was purged by N₂ before the reaction. Then 0.38 ml of 98% FA was injected into the catalyst solution at room temperature. The gas molecules produced were analyzed by a gas chromatograph. The amount of gas (H₂ + CO₂) evolution during the photocatalytic reaction was evaluated by a gas burette system. The TOFs are calculated within the initial 10 min conforming to the subsequent Eq. ³²:

$$TOF = n_{gas\ produced} / (n_{AgPd} \times h)$$

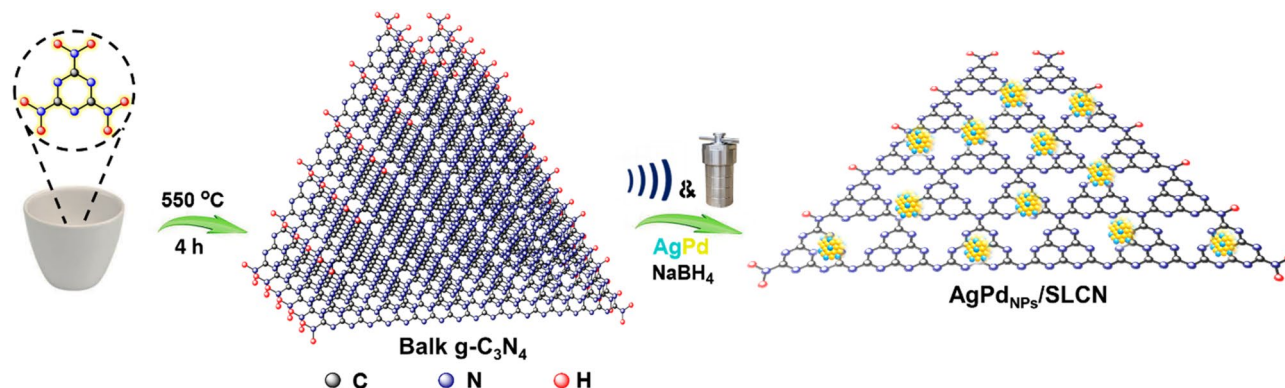


Figure 1. Schematic illustration for the synthesis of AgPd_{NPs}/SLCN.

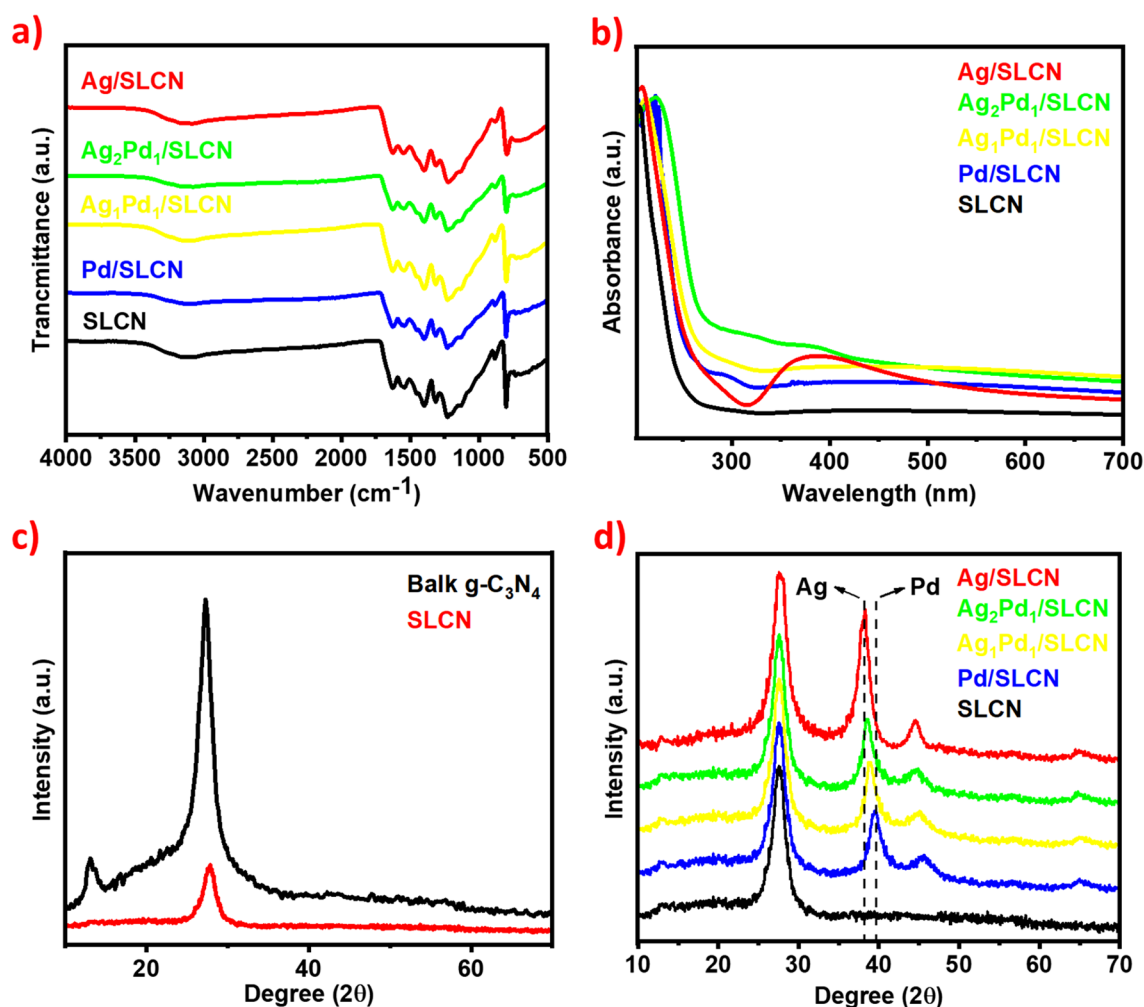


Figure 2. (a) FT-IR spectrum, (b) UV-vis spectra of SLCN, Ag/SLCN, Ag₂Pd₁/SLCN, Ag₁Pd₁/SLCN and Pd/SLCN, (c) XRD patterns of the bulk g-C₃N₄ and SLCN, (d) XRD patterns of SLCN, Ag/SLCN, Ag₂Pd₁/SLCN, Ag₁Pd₁/SLCN and Pd/SLCN.

Results and discussion

As shown in Fig. 1, we constructed the Mott-Schottky junction based ultra-thin carbon nitride single layers decorated with AgPd alloy nanoparticles with a simple strategy through a strong interaction between AgPd_{NPs} and SLCN toward enhancement photocatalytic dehydrogenation of FA.

The chemical structure of SLCN as well as SLCN decorated with AgPd nanoparticles was analyzed by FT-IR spectrum (Fig. 2a). The band appeared at 809 cm⁻¹ is ascribed to the specific breathing mode of the triazine ring.

Multiple peaks in the proximity to each other and in the range of 1200–1700 cm^{-1} are related to the stretching modes of aromatic C–N heterocycles. Wide absorption in the area of 3000–3500 cm^{-1} is attributed to the N–H stretching mode⁷¹. UV–vis absorption spectra of $\text{AgPd}_{\text{NPs}}/\text{SLCN}$ samples were inspected (Fig. 2b). For Ag nanoparticles, the LSPR with high intensity in a region of 390–410 nm is observed. In the case of AgPd alloy, the intensity of the peak's changes with a change in the Ag:Pd ratio, so that for a ratio of 1:1 compared to 2:1, the effect of LSPR shows a greater reduction, which can be due to charge transfer to the Ag_{NPs} surface^{37,72–74}. XRD planes of the bulk $g\text{-C}_3\text{N}_4$, SLCN and AgPd alloy nanoparticles supported on SLCN with different Ag:Pd ratios were revealed in Fig. 2c,d. For bulk $g\text{-C}_3\text{N}_4$, a slight peak at 13.1° is observed, which is assigned to the (100) plane, attribute to the in-plane structural packaging motif of tri-s-triazine units. The strong diffraction at 27.5° also belongs to the (002) plane, which is related to the accumulation between the inter-layer stacking of conjugated aromatic rings. The peak with low intensity at 27.5° is related to the SLCN, which indicates the interlayer structure of bulk CN was annihilated after exfoliation⁷¹. For AgPd alloy nanoparticles with different ratios, the peak appears at a 39°, which shifted to elder angles with increasing Pd:Ag ratio, signifying that the AuPd alloy is formed on SLCN³¹. The nitrogen adsorption–desorption isotherms for SLCN show type III isotherms (Fig. S1). The specific surface area of SLCN is 88.05 m^2/g , which is 14.5 times larger than bulk $g\text{-C}_3\text{N}_4$ (6.06 m^2/g). The pore size distribution of BJH shows an average pore diameter of 1.64 and 14.37 nm for SLCN and 12.24 nm for bulk CN (Fig. S2). The high specific surface area and large total pore volume indicate that SLCN has a nanoporous structure, leading to increased photocatalytic performance through favorable mass transfer.

Figure 3a demonstrates the general spectrum of $\text{Ag}_2\text{Pd}_1/\text{SLCN}$ in which the characteristic peaks C 1 s, N 1 s, Ag 3d and Pd 3d are clearly visible. In the high-resolution XPS spectrum for the C element, the binding energy at 284.7 eV is attributed to the C–C bond and at 288 eV to C=N–C at SLCN (Fig. 3b)^{75–77}. Figure 3c also shows the XPS spectrum of element N in $\text{Ag}_2\text{Pd}_1/\text{SLCN}$, which corresponds to the energy bands C–N–C and C=N–H and –C=N^{75–77}. Photoelectron spectroscopy (XPS) analysis was executed to further explore the effect of SLCN on the electronics of Ag and Pd structures in $\text{Ag}_2\text{Pd}_1/\text{SLCN}$. Examination of the XPS spectra of Ag 3d and Pd 3d shows that the binding energies for Pd 3d_{3/2} in $\text{Ag}_2\text{Pd}_1/\text{SLCN}$ is shifted to lower values due to the handover of electrons from SLCN and Ag to Pd, while the binding energies for Ag 3d_{3/2} in $\text{Ag}_2\text{Pd}_1/\text{SLCN}$ shift to higher values (Fig. 3d,e)^{31,35,78}. In fact, this indicates the redistribution of charge from higher Fermi level (Ag) to lower Fermi level (Pd)³¹. According to XPS analysis, the atomic percentages of elements in $\text{Ag}_2\text{Pd}_1/\text{SLCN}$ for C, N, O, Ag and Pd are 32.82%, 60.04%, 6.52%, 0.42% and 0.2%, respectively.

Figure 4a–d exhibitions the SEM image of the bulk $g\text{-C}_3\text{N}_4$ and SL-CN after ultrasonic exfoliation and then hydrothermal procedure. The presence of many sheets with laminar morphology proves SLCN synthesis. The SEM–EDS image and elemental mapping images approve the attendance of all composing elements (C, N, Ag, Pd) in the $\text{Ag}_2\text{Pd}_1/\text{SLCN}$ structure (Fig. 4f–j). Figure 4e displays the EDS–SEM line scan profiles of $\text{Ag}_2\text{Pd}_1/\text{SLCN}$ containing C, N, Ag and Pd atoms, which clearly confirm the approximately homogeneous distribution of atoms.

The TEM image and related particle size histogram for SLCN and $\text{AgPd}_{\text{NPs}}/\text{SLCN}$ (Ag: Pd in a ratio of 1: 1) is revealed in Fig. 5a–d. As is clear, a single-layer structure is beheld for the SLCN, which is also concord with the SEM image. The TEM image also shows 6 nm spherical AgPd_{NPs} that are well embedded on the surface of SLCN.

The photoluminescence (PL) spectra (excitation under 325 nm) for SLCN and $\text{Ag}_1\text{Pd}_1/\text{SLCN}$ are provided in Fig. S2. The PL intensity of $\text{Ag}_1\text{Pd}_1/\text{SLCN}$, is lower than that of SLCN, indicating that compared to SLCN, photo-generated electron transfer in $\text{Ag}_1\text{Pd}_1/\text{SLCN}$ accelerates faster and diminishes the electron recombination rate of electrons and holes. Compared to SLCN and $\text{Ag}_1\text{Pd}_1/\text{SLCN}$, the peak intensity is higher for $g\text{-C}_3\text{N}_4$, which indicates that the recombination rate of electrons and holes is higher (Fig. S3). UV–DRS measurement was also performed to evaluate the optical absorption properties of SLCN and $\text{Ag}_1\text{Pd}_1/\text{SLCN}$ (Fig. S4). For SLCN, low absorption between 450 and 700 nm is observed, indicating the poor performance of SLCN in visible light. After modification of SLCN with AgPd nanoparticles, the absorption of visible light increased slightly, indicating the acceptable performance of $\text{Ag}_1\text{Pd}_1/\text{SLCN}$ in visible light. Also, the presence of poor absorption in the range of 450–600 nm could be related to the localized surface plasma resonance (LSPR) effect of silver nanoparticles on the surface of SLCN.

The optical bandgap for the photocatalysts was obtained using the Tauc's equation⁷⁹:

$$\alpha h\nu = A(h\nu - E_g)^n$$

α : is the absorption coefficient. E_g : band gap. h : Planck's constant. ν : the frequency of light. n : the electron transition process constant (the value of n is considered to be as 1/2). A : constant (in the ideal case $A = 1$).

For each of the desired photocatalysts, the optical energy bandgap was appointed by extrapolation of the lined area of the plot of $(\alpha h\nu)^2$ versus $h\nu$ (Fig. 6a–d).

Catalytic H_2 evolution for 10 mL of 1.0 M aqueous FA was tested for all synthesized samples in the utilization of 0.2 g of the catalyst under dark conditions at ambient temperature. No gas was produced for SLCN or Ag/SLCN . In comparison, when Pd/SLCN, AgPd/SLCN were used, gas release was observed within 60 min, which the highest production value (15 mL) was obtained for Pd/SLCN (Fig. 7a). Examination of the above conditions under visible light irradiation showed a comparable increased activity compared to the dark conditions for all Pd-comprising photocatalysts. Among the bimetallic photocatalysts for the 1: 1 ratio of Ag/Pd, the amount of gas produced was 50 mL, which shows the highest evolution rate compared to the 1: 3 and 3: 1 ratio (39 and 28 mL, respectively) (Fig. 7b). Specifically, the activity of bimetallic AgPd_{NPs} photocatalysts is superior to that of Pd_{NPs} under the same situations. This can be credited to the higher activity of AgPd alloys which occurs as a result of stout-interplay and charge redistribution betwixt Ag and Pd and thus accelerate the photocatalytic dehydrogenation of FA. Figure 7c illustrations the TOFs value versus the ratio of Ag:Pd for the SLCN-supported photocatalysts in both dark and visible light conditions. Specifically, $\text{Ag}_1\text{Pd}_1/\text{SLCN}$ disclosed the utmost activity with a TOF value of 224 h^{-1} under visible light irradiation. The highest TOF value in the dark condition was

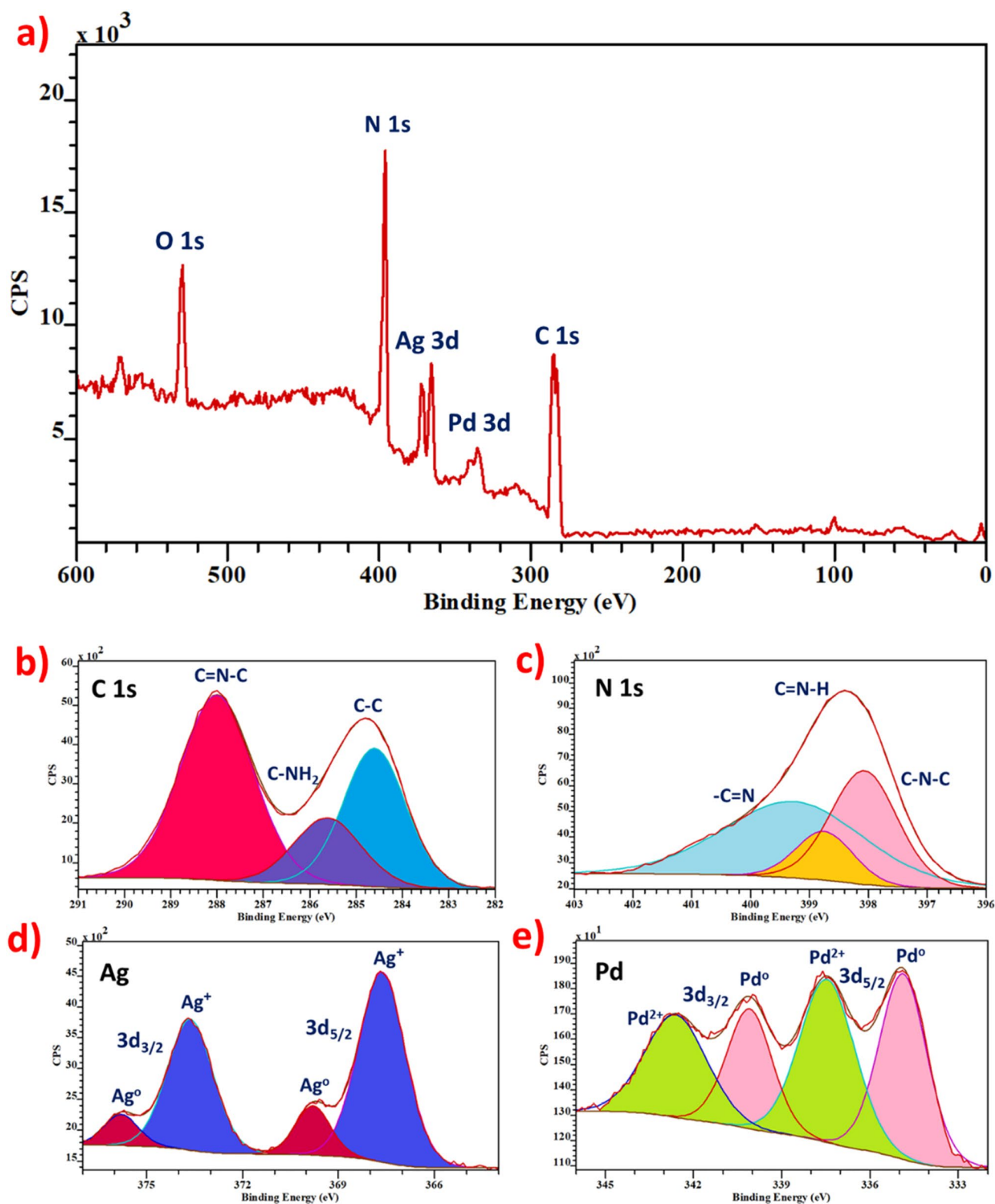


Figure 3. (a) general XPS of Ag₂Pd₁/SLCN, (b) C1s regions of Ag₂Pd₁/SLCN, (c) N1s regions of Ag₂Pd₁/SLCN (d), Ag 3d regions of Ag₂Pd₁/SLCN and (e) Pd 3d regions of Ag₂Pd₁/SLCN.

also obtained for Pd/SLCN, which was equal to 53 h⁻¹. The results specify that alloying Ag with Pd leads to a synergistic effect and thus increases the activity of the desired photocatalyst. Accordingly, Ag₁Pd₁/SLCN was the best photocatalyst among the catalysts we studied for the evolution of hydrogen from the FA.

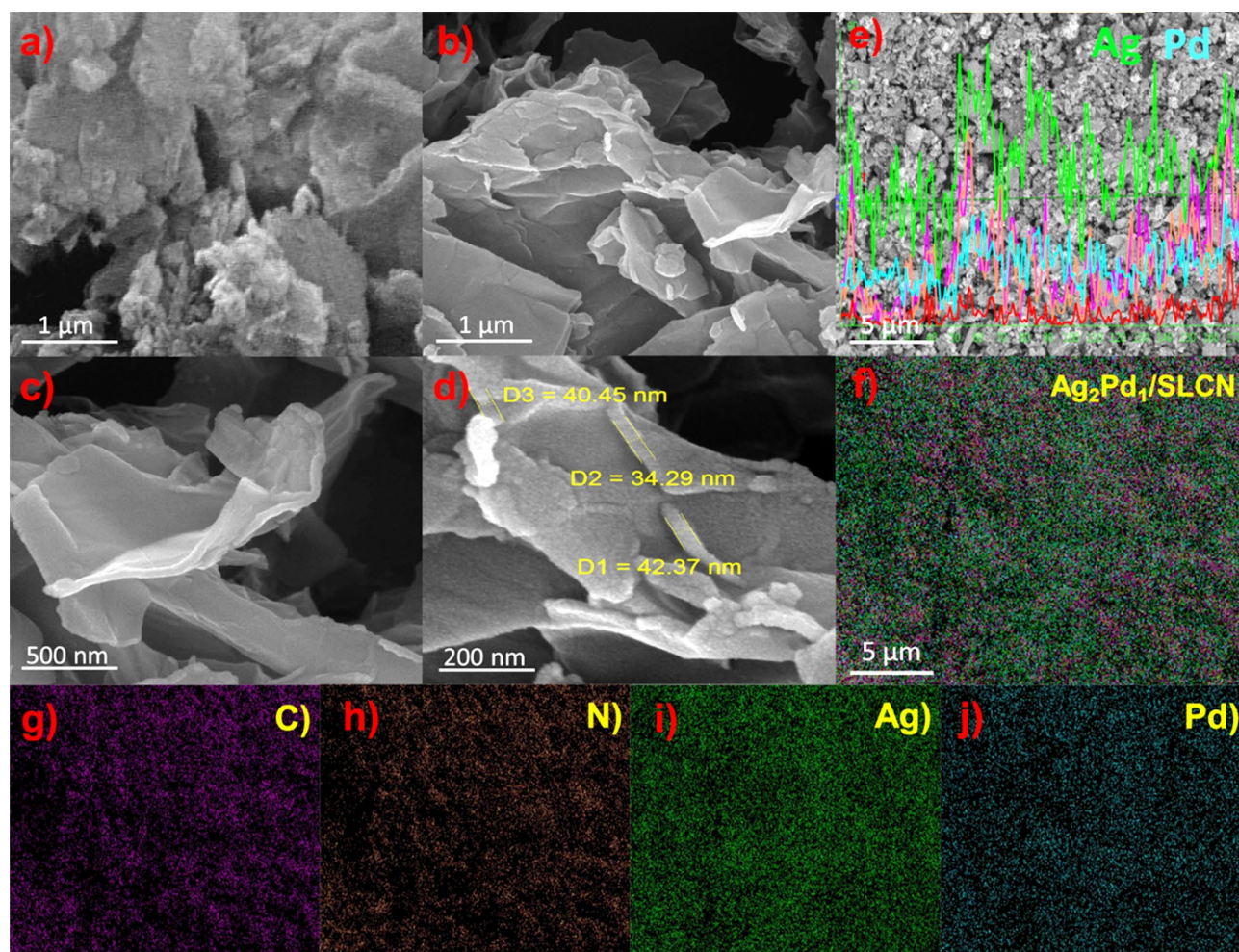


Figure 4. (a) SEM images of bulk $g\text{-C}_3\text{N}_4$, (b, c and d) SEM images of SLCN, (e) EDS-SEM line scan profiles of $\text{Ag}_2\text{Pd}_1/\text{SLCN}$, (f) general map of $\text{Ag}_2\text{Pd}_1/\text{SLCN}$ and (g–j) elemental mappings of SEM-EDX mappings of $\text{Ag}_2\text{Pd}_1/\text{SLCN}$.

Support of AgPd alloy on bulk carbon nitride ($\text{Ag}_1\text{Pd}_1/g\text{-C}_3\text{N}_4$) was evaluated to investigate the Mott-Schottky effect on photocatalytic performance compared to $\text{Ag}_1\text{Pd}_1/\text{SLCN}$. As shown in Fig. 8a, less gas evolution (38 mL) was observed for $\text{Ag}_1\text{Pd}_1/g\text{-C}_3\text{N}_4$ under light irradiation. It is clear that the catalytic performance of $\text{Ag}_1\text{Pd}_1/\text{SLCN}$ is higher than that of $\text{Ag}_1\text{Pd}_1/g\text{-C}_3\text{N}_4$, mainly owing to the large specific surface area of the SLCN, which effectively shortens the electron transfer path between the support and the AgPd. For $\text{Ag}_1\text{Pd}_1/g\text{-C}_3\text{N}_4$ the photocatalytic activity with a TOF value of 178 h^{-1} was obtained as shown in Fig. 8b.

Based on the above findings, we focused our studies in line with the influence of different amounts of $\text{Ag}_1\text{Pd}_1/\text{SLCN}$ catalysts for the photocatalytic evolution of hydrogen. Accordingly, we tested values of less and more than 20 mg of $\text{Ag}_1\text{Pd}_1/\text{SLCN}$ catalyst for achieving a better result. Using the values of 5 and 10 mg of catalyst showed less gas evolution. For 30 mg of the catalyst, a similar result was obtained with the amount of 20 mg catalyst (Fig. 9a). In the following, by achieving the optimal amount of catalyst, we also studied the effect of different concentrations of FA. It is necessary to mention this point, we performed all of our studies at a concentration of 1 M, 10 mL of formic acid in accordance with valid reports in the literature. However, due to our interest in completing our research results, we also evaluated different concentrations of formic acid. At low concentrations, for example, 0.25 and 0.5 M, the amount of gas production was lower (20 and 30 mL, respectively), while at a concentration of 2 M, the amount of gas produced was 51 mL. This specifies that for high concentrations the evolution of hydrogen with increased intensity is not observed (Fig. 9b). The rate of photocatalytic dehydrogenation of FA augmented linearly with increasing concentration (Fig. 9c).

In the next step, the effect of light intensity on photo-decomposition of FA was explored using $\text{Ag}_1\text{Pd}_1/\text{SLCN}$ and it was observed that the rate of dehydrogenation of FA enlarged linearly with increment light intensity (Fig. 10a,b).

To ascertain the molar ratio of $\text{CO}_2:\text{H}_2$, a NaOH trap (10 M NaOH based on a gas burette system) was utilized to absorb CO_2 ^{35,80}. In this experiment, the gas mixture produced was passed through a NaOH trap. The volume of gas produced in the use of the NaOH trap was reduced by half compared to the state without traps, which indicates that the volume of gas produced is 1: 1 (Fig. 11).

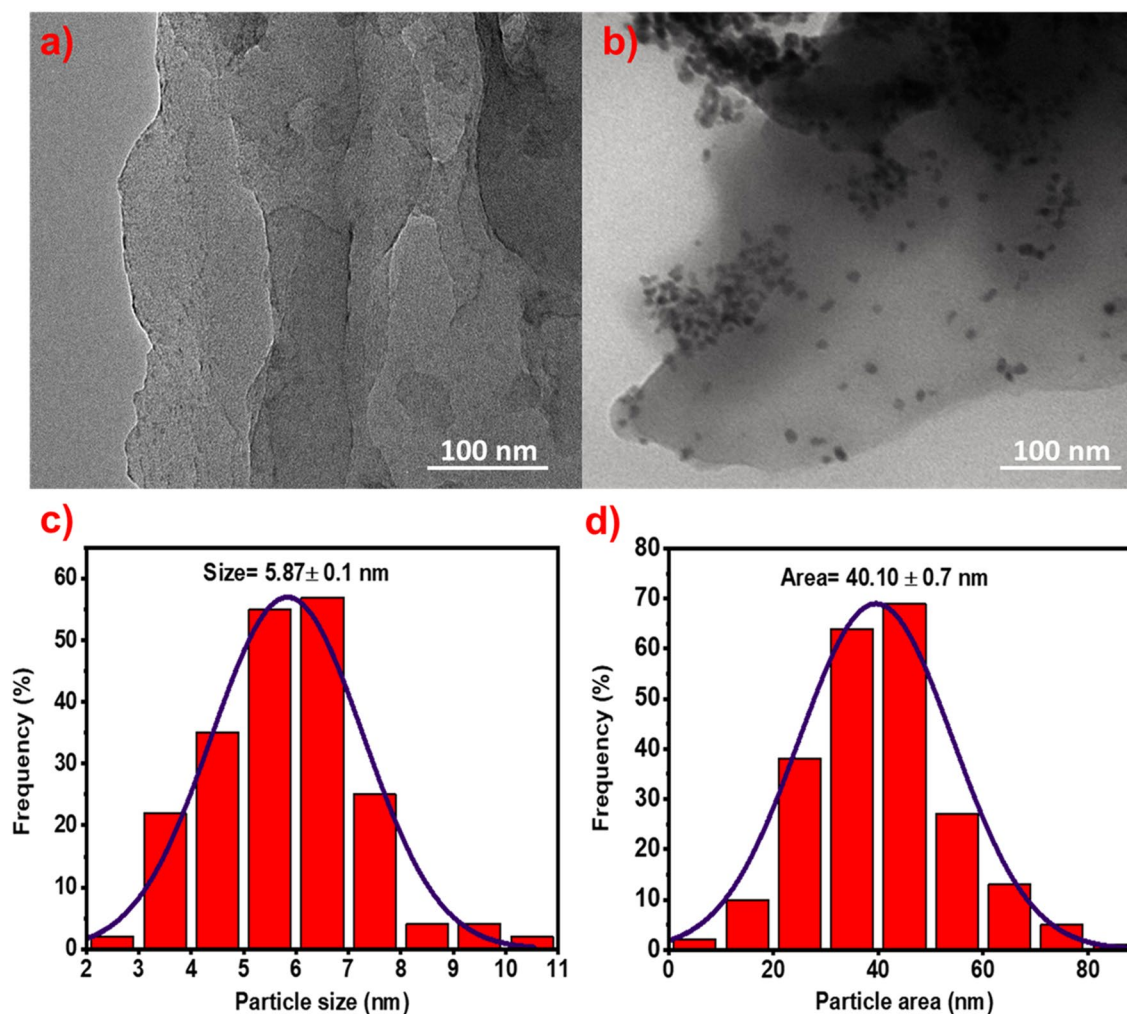


Figure 5. (a) TEM image of SLCN, (b) TEM image of Ag₁Pd₁/SLCN, (c) the average diameter histogram of AgPd_{NPs} for Ag₁Pd₁/SLCN and (d) the average particle area histogram of AgPd_{NPs} for Ag₁Pd₁/SLCN.

The activation energy ($E_a = +31.2 \text{ kJmol}^{-1}$) of reaction for Ag₁Pd₁/SLCN catalyst was calculated from the ($\ln \text{TOF} = -E_a/R + (1/T) + \ln A$, $R = 8.314 \text{ J/mol. K}$) relationship (Fig. 12b). The value of R-square 0.97 was attained, which indicates that the points are the lined trend line.

Ag₁Pd₁/SLCN activity after four times exposure to visible light exposed that this catalyst is entirely stable and recyclable below visible light irradiation (Fig. 13).

Table 1 summarizes the results of our work compared to AgPd/C₃N₄-based photocatalysts previously reported in the literature. As can be seen, the Ag₁Pd₁/SLCN photocatalyst with active sites, showed acceptable catalytic activity relative to the reported works.

Conclusions

In summary, a series of AgPd alloy nanoparticles decorated on an SLCN semiconductor surface was designed to optimize plasmonic Mott-Schottky catalysts toward the competent evolution of photocatalytic hydrogen from FA. Exhaustive studies revealed that the being of coordinated unsaturated N atoms on the SLCN surface is indispensable for the concurrent stabilization of Ag and Pd as uniform alloy nanoparticles. On the other hand, the desirable charge handover from SLCN and Ag to Pd leads to the enrichment of Pd with electrons and thus affords more catalytic activity and stability for the H₂ evolution below visible light. This study presents a new path for designing plasmonic Mott-Schottky heterogeneous catalysts with synergistic effects and high efficiency for photocatalytic hydrogen evolution by using formic acid.

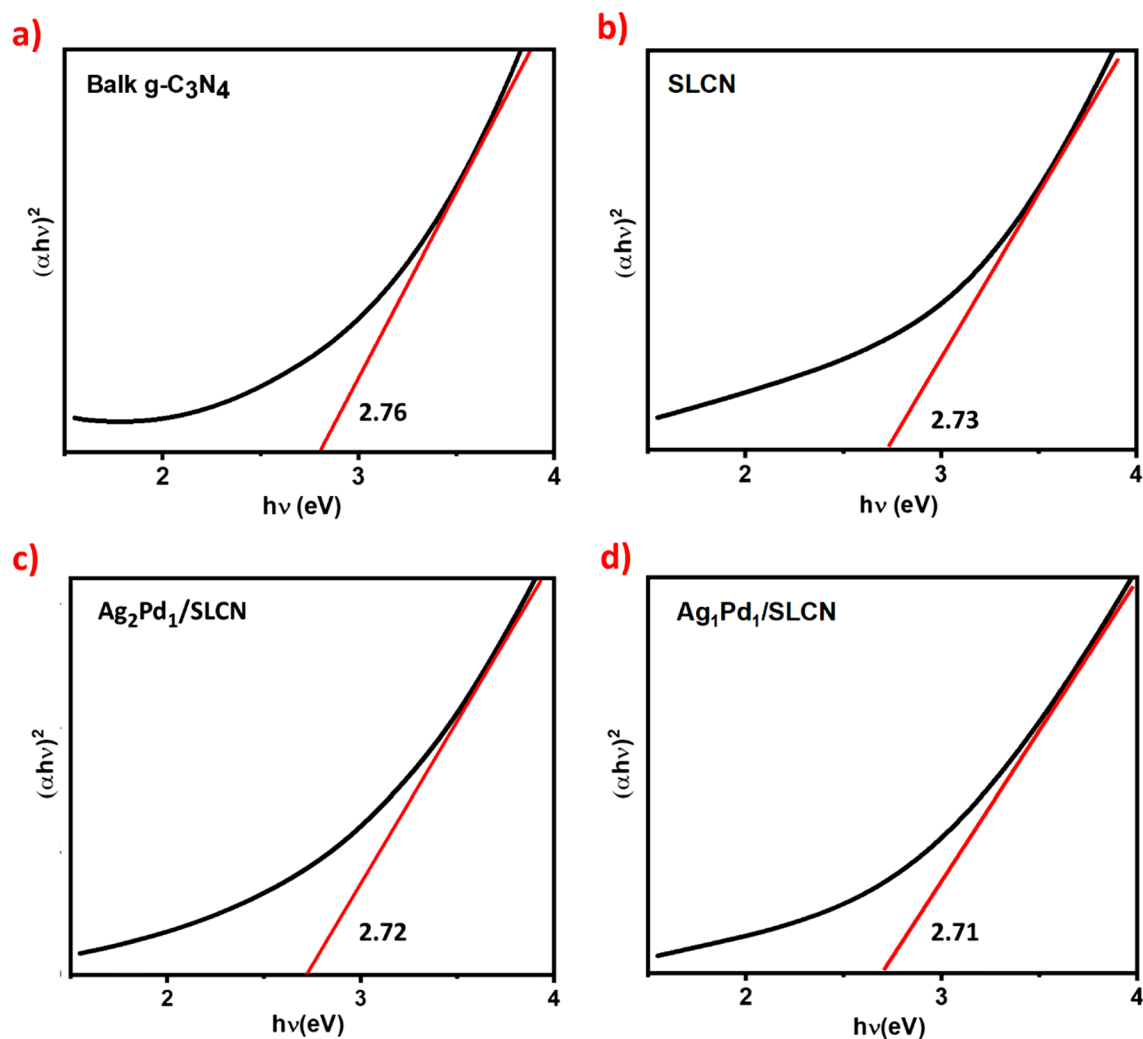


Figure 6. (a–d) plots of $(\alpha h\nu)^2$ versus $h\nu$ for bulk $g\text{-C}_3\text{N}_4$, SLCN, $\text{Ag}_2\text{Pd}_1/\text{SLCN}$ and $\text{Ag}_1\text{Pd}_1/\text{SLCN}$.

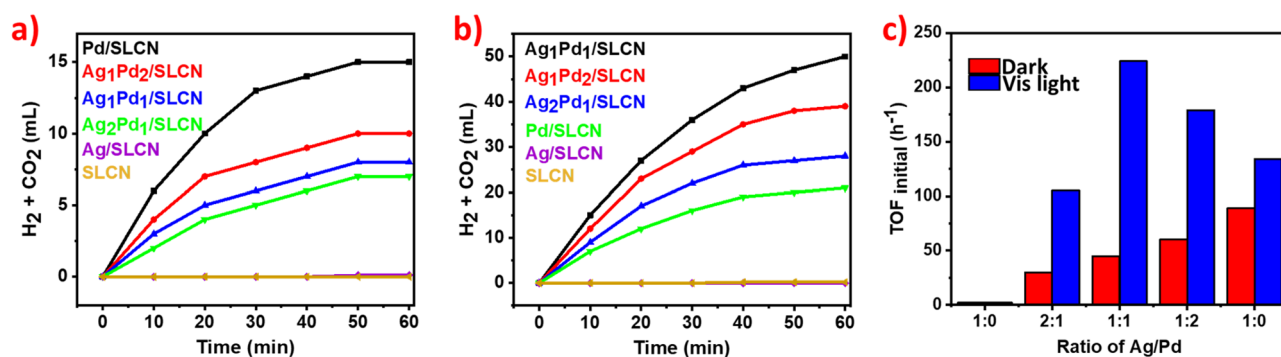


Figure 7. (a) Time-dependent gas evolution plots from FA in the dark at $\sim 30^\circ\text{C}$, (b) in the light irradiation at $\sim 30^\circ\text{C}$ and (c) the TOFs ratio of various catalysts in the dark and light irradiation.

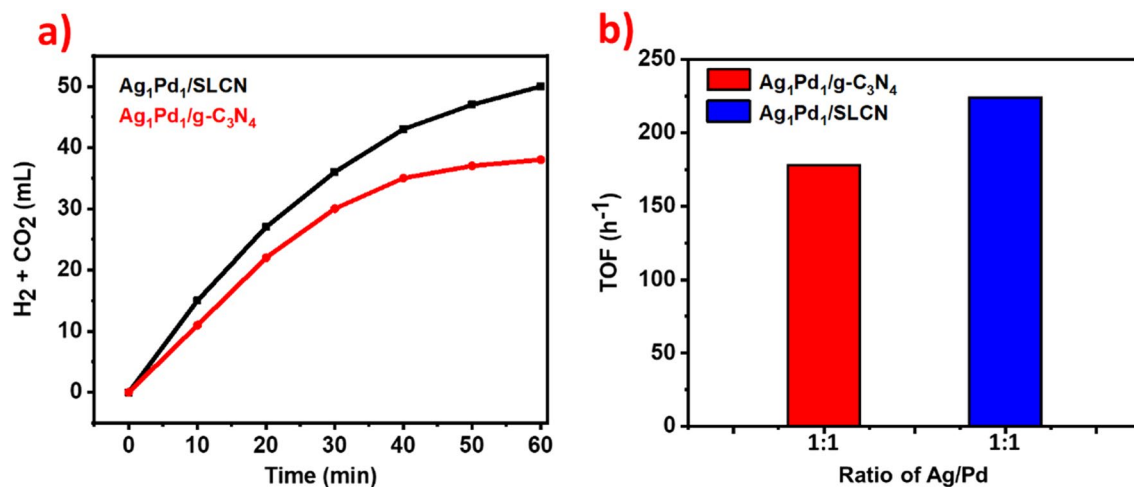


Figure 8. (a) Time-dependent gas evolution plots from FA in the light irradiation at ~30 °C for Ag₁Pd₁/SLCN versus Ag₁Pd₁/g-C₃N₄ (b) the TOFs ratio of Ag₁Pd₁/SLCN versus Ag₁Pd₁/g-C₃N₄ in the light irradiation.

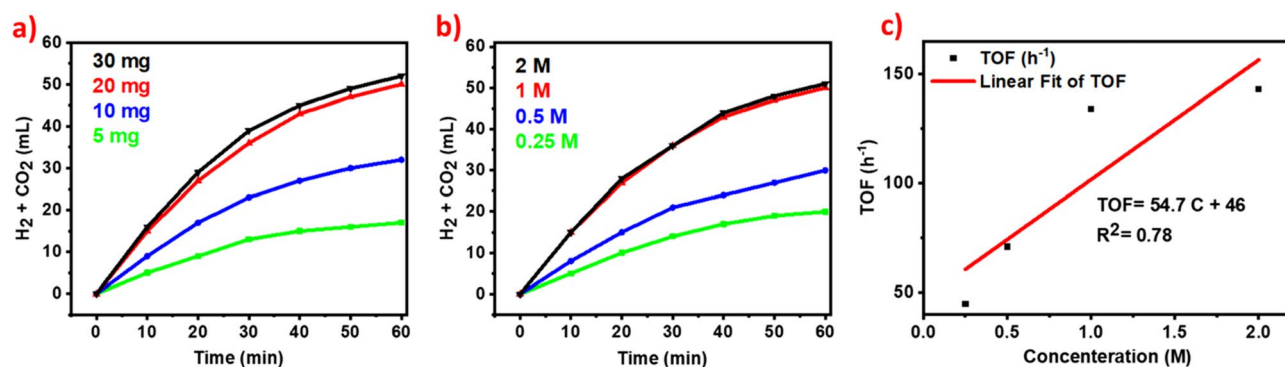


Figure 9. (a) The volume of gas evolution in the use of different amount of Ag₁Pd₁/SLCN for the photo-decomposition of FA, (b) the volume of gas evolution in the use of different concentrations for the photocatalytic decomposition of FA and (c) Initial TOF versus concentrations for Ag₁Pd₁/SLCN under light irradiation.

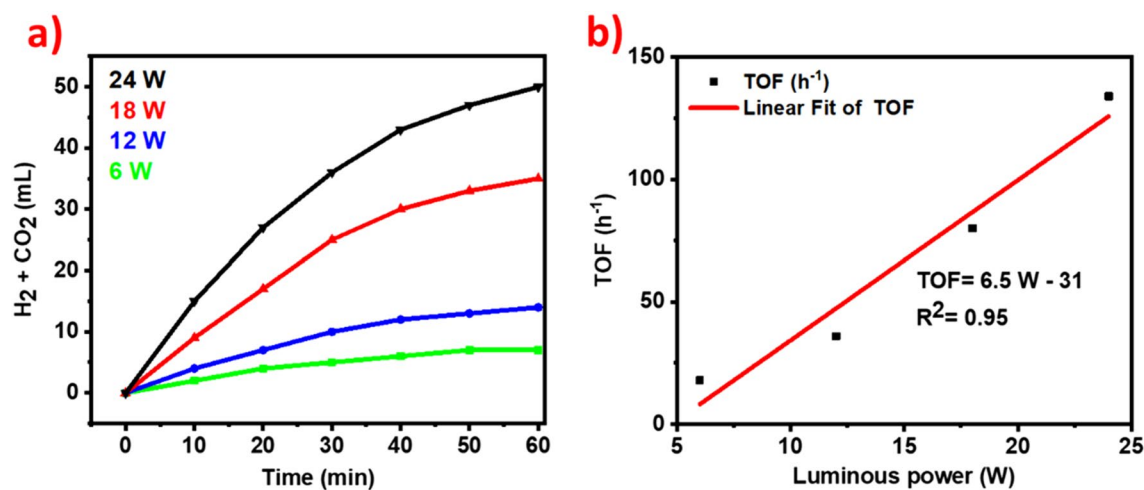


Figure 10. (a) The volume of gas evolution in the use of different light intensities for the photocatalytic decomposition of FA and (b) Initial TOF versus luminous power for Ag₁Pd₁/SLCN under visible light irradiation.

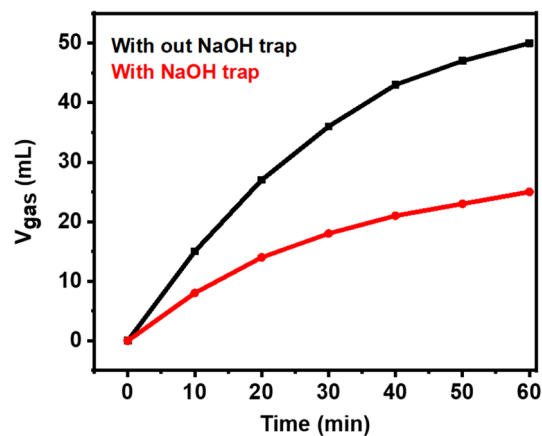


Figure 11. The comparison of the volume of gas produced by using $\text{Ag}_1\text{Pd}_1/\text{SLCN}$ for dehydrogenation of aqueous FA solution with and without NaOH trap under visible light irradiation.

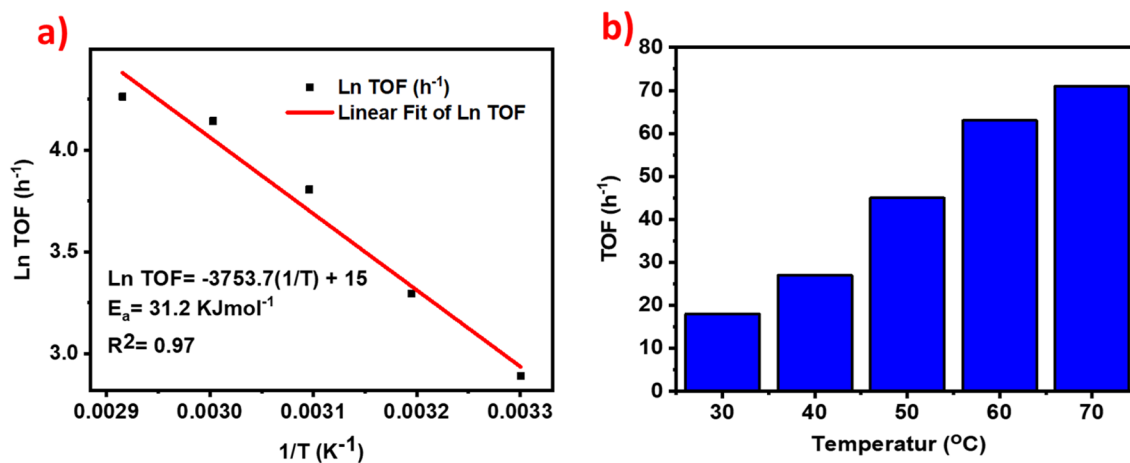


Figure 12. (a) Ln TOF versus $1/T$ plot in course of FA dehydrogenation by $\text{Ag}_1\text{Pd}_1/\text{SLCN}$ at diverse temperatures, (b) Initial TOF versus temperatures plot for $\text{Ag}_1\text{Pd}_1/\text{SLCN}$.

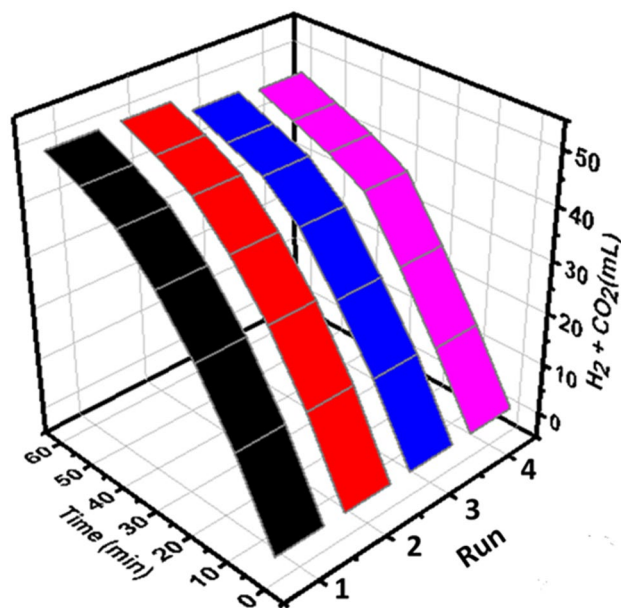


Figure 13. The recycling capability of Ag₁Pd₁/SLCN below visible light irradiation.

Entry	Catalyst	Lamp	T (°C)	TOF (h ⁻¹)	V _{gas} (mL)	Ref
1	AgPd/CN	300 W Xenon	30	254	25	³¹
2	PdAg@g-C ₃ N ₄	300 W Xenon	25	420	330	³⁵
3	AgPd/2D CNNs	300 W Xenon	50	2936.8	135	⁴²
4	AgPd/SLCN	24 W LED-SMD	30	224	50	This work

Table 1. Comparison of different AgPd/C₃N₄-based photocatalysts for H₂ evolution.

Data availability

All data generated or analysed during this study are included in this published article (and its Supplementary Information files).

Received: 26 February 2022; Accepted: 22 July 2022

Published online: 09 August 2022

References

- Tian, Y., Liu, X., Chen, F. & Zheng, Y. Harvesting energy from sun, outer space, and soil. *Sci. Rep.* **10**, 1–9 (2020).
- Vavilapalli, D. S. *et al.* Nitrogen incorporated photoactive brownmillerite Ca₂Fe₂O₅ for energy and environmental applications. *Sci. Rep.* **10**, 1–13 (2020).
- Chu, S. & Majumdar, A. Opportunities and challenges for a sustainable energy future. *Nature* **488**, 294–303 (2012).
- Luo, J. *et al.* Water photolysis at 12.3% efficiency via perovskite photovoltaics and Earth-abundant catalysts. *Science* **345**, 1593–1596 (2014).
- Cabán-Acevedo, M. *et al.* Efficient hydrogen evolution catalysis using ternary pyrite-type cobalt phosphosulphide. *Nat. Mater.* **14**, 1245–1251 (2015).
- Sanderson, K. Hydrogen fuel goes liquid. *Nature* **748**, 70820 (2007).
- Van Noorden, R. Liquid storage could make hydrogen a feasible fuel. *Nature* <https://doi.org/10.1038/nature.2013.12518> (2013).
- Staffell, I. *et al.* The role of hydrogen and fuel cells in the global energy system. *Energy Environ. Sci.* **12**, 463–491 (2019).
- Eppinger, J. & Huang, K. W. Formic acid as a hydrogen energy carrier. *ACS Energy Lett.* **2**, 188–195 (2017).
- Grasemann, M. & Laurenczy, G. Formic acid as a hydrogen source - Recent developments and future trends. *Energy Environ. Sci.* **5**, 8171–8181 (2012).
- Joó, F. Breakthroughs in hydrogen storage\formic acid as a sustainable storage material for hydrogen. *ChemSuschem* **1**, 805–808 (2008).
- Fellay, C., Dyson, P. J. & Laurenczy, G. A viable hydrogen-storage system based on selective formic acid decomposition with a ruthenium catalyst. *Angew. Chemie - Int. Ed.* **47**, 3966–3968 (2008).
- Enthaler, S., Von Langermann, J. & Schmidt, T. Carbon dioxide and formic acid - The couple for environmental-friendly hydrogen storage?. *Energy Environ. Sci.* **3**, 1207–1217 (2010).
- Boddien, A. *et al.* Efficient dehydrogenation of formic acid using an iron catalyst. *Science* **333**, 1733–1736 (2011).
- Kar, S., Rauch, M., Leitus, G., Ben-David, Y. & Milstein, D. Highly efficient additive-free dehydrogenation of neat formic acid. *Nat. Catal.* **4**, 193–201 (2021).
- Zhu, Q. L., Tsumori, N. & Xu, Q. Immobilizing extremely catalytically active palladium nanoparticles to carbon nanospheres: A weakly-capping growth approach. *J. Am. Chem. Soc.* **137**, 11743–11748 (2015).

17. Zhang, S. *et al.* Photocatalytic hydrogen evolution from formate and aldehyde over molecular iridium complexes stabilized by bipyridine-bridging organosilica nanotubes. *Appl. Catal. B Environ.* **236**, 466–474 (2018).
18. Nielsen, M. *et al.* Low-temperature aqueous-phase methanol dehydrogenation to hydrogen and carbon dioxide. *Nature* **495**, 85–89 (2013).
19. Verma, P., Yuan, K., Kuwahara, Y., Mori, K. & Yamashita, H. Enhancement of plasmonic activity by Pt/Ag bimetallic nanocatalyst supported on mesoporous silica in the hydrogen production from hydrogen storage material. *Appl. Catal. B Environ.* **223**, 10–15 (2018).
20. Hu, H., Jiao, Z., Ye, J., Lu, G. & Bi, Y. Highly efficient hydrogen production from alkaline aldehyde solutions facilitated by palladium nanotubes. *Nano Energy* **8**, 103–109 (2014).
21. Yurderi, M., Bulut, A., Zahmakiran, M. & Kaya, M. Carbon supported trimetallic PdNiAg nanoparticles as highly active, selective and reusable catalyst in the formic acid decomposition. *Appl. Catal. B Environ.* **160–161**, 514–524 (2014).
22. Zhang, S., Metin, Ö., Su, D. & Sun, S. Monodisperse AgPd alloy nanoparticles and their superior catalysis for the dehydrogenation of formic acid. *Angew. Chemie - Int. Ed.* **52**, 3681–3684 (2013).
23. Wang, Z. L., Yan, J. M., Wang, H. L., Ping, Y. & Jiang, Q. Pd/C synthesized with citric acid: An efficient catalyst for hydrogen generation from formic acid/sodium formate. *Sci. Rep.* **2**, 1–6 (2012).
24. Sordakis, K. *et al.* Homogeneous catalysis for sustainable hydrogen storage in formic acid and alcohols. *Chem. Rev.* **118**, 372–433 (2018).
25. Mellmann, D., Sponholz, P., Junge, H. & Beller, M. Formic acid as a hydrogen storage material-development of homogeneous catalysts for selective hydrogen release. *Chem. Soc. Rev.* **45**, 3954–3988 (2016).
26. Mori, K., Futamura, Y., Masuda, S., Kobayashi, H. & Yamashita, H. Controlled release of hydrogen isotope compounds and tunneling effect in the heterogeneously-catalyzed formic acid dehydrogenation. *Nat. Commun.* **10**, 1–10 (2019).
27. Mori, K., Sano, T., Kobayashi, H. & Yamashita, H. Surface engineering of a supported PdAg catalyst for hydrogenation of CO₂ to formic acid: elucidating the active Pd atoms in alloy nanoparticles. *J. Am. Chem. Soc.* **140**, 8902–8909 (2018).
28. Farajzadeh, M., Alamgholilo, H., Nasibipour, F., Banaei, R. & Rostamnia, S. Anchoring Pd-nanoparticles on dithiocarbamate-functionalized SBA-15 for hydrogen generation from formic acid. *Sci. Rep.* **10**, 1–9 (2020).
29. Jin, M. H. *et al.* Mesoporous silica supported Pd-MnOx catalysts with excellent catalytic activity in room-temperature formic acid decomposition. *Sci. Rep.* **6**, 1–12 (2016).
30. van Putten, R., Wissink, T., Swinkels, T. & Pidko, E. A. Fuelling the hydrogen economy: Scale-up of an integrated formic acid-to-power system. *Int. J. Hydrogen Energy* **44**, 28533–28541 (2019).
31. Xiao, L. *et al.* Carbon nitride supported AgPd alloy nanocatalysts for dehydrogenation of formic acid under visible light. *J. Mater. Chem. A* **5**, 6382–6387 (2017).
32. Zhang, S. *et al.* Plasmonic AuPd-based Mott-Schottky photocatalyst for synergistically enhanced hydrogen evolution from formic acid and aldehyde. *Appl. Catal. B Environ.* **252**, 24–32 (2019).
33. Liu, P. *et al.* Visible-light-driven catalytic activity enhancement of Pd in AuPd nanoparticles for hydrogen evolution from formic acid at room temperature. *Appl. Catal. B Environ.* **204**, 497–504 (2017).
34. Wen, M., Mori, K., Kuwahara, Y. & Yamashita, H. Plasmonic Au@Pd nanoparticles supported on a basic metal-organic framework: Synergic boosting of H₂ production from formic acid. *ACS Energy Lett.* **2**, 1–7 (2017).
35. Liu, H. *et al.* Photocatalytic dehydrogenation of formic acid promoted by a superior PdAg@g-C₃N₄ Mott-Schottky heterojunction. *J. Mater. Chem. A* **7**, 2022–2026 (2019).
36. Niu, W. *et al.* Enhancing electron transfer and electrocatalytic activity on crystalline carbon-conjugated g-C₃N₄. *ACS Catal.* **8**, 1926–1931 (2018).
37. Zou, W. *et al.* Advantageous interfacial effects of AgPd/g-C₃N₄ for photocatalytic hydrogen evolution: Electronic structure and H₂O dissociation. *Chem. - A Eur. J.* **25**, 5058–5064 (2019).
38. Fan, X. *et al.* Construction of conjugated intramolecular for donor-acceptor copolymers Photocatalytic hydrogen evolution. 1–24.
39. Altan, O., Altintas, E., Alemdar, S. & Metin, Ö. The rational design of a graphitic carbon nitride-based dual S-scheme heterojunction with energy storage ability as a day/night photocatalyst for formic acid dehydrogenation. *Chem. Eng. J.* **441**, 136047 (2022).
40. Altan, O. & Metin, Ö. Boosting formic acid dehydrogenation via the design of a Z-scheme heterojunction photocatalyst: The case of graphitic carbon nitride/Ag/Ag₃PO₄-AgPd quaternary nanocomposites. *Appl. Surf. Sci.* **535**, 147740 (2021).
41. Li, X. H. Metal nanoparticles at mesoporous N-doped carbons and carbon nitrides: Functional Mott-Schottky heterojunctions for catalysis. *Chem. Soc. Rev.* **42**(16), 6593–6604. <https://doi.org/10.1039/c3cs60067j> (2013).
42. Wan, C. *et al.* Boosting visible-light-driven hydrogen evolution from formic acid over. *Chem. Eng. J.* **396**, 125229 (2020).
43. Cao, S. & Yu, J. g-C₃N₄-based photocatalysts for hydrogen generation. *J. Phys. Chem. Lett.* **5**, 2101–2107 (2014).
44. Prasad, C. *et al.* A latest overview on photocatalytic application of g-C₃N₄ based nanostructured materials for hydrogen production. *Int. J. Hydrogen Energy* **45**, 337–379 (2020).
45. Su, K. *et al.* G-c₃n₄ derived materials for photocatalytic hydrogen production: A mini review on design strategies. *J. Renew. Mater.* **10**, 653–663 (2022).
46. Liao, G. *et al.* Semiconductor polymeric graphitic carbon nitride photocatalysts: the “holy grail” for the photocatalytic hydrogen evolution reaction under visible light. *Energy Environ. Sci.* **12**(7), 2080–2147. <https://doi.org/10.1039/C9EE00717B> (2019).
47. Ong, W. J., Tan, L. L., Ng, Y. H., Yong, S. T. & Chai, S. P. Graphitic carbon nitride (g-C₃N₄)-based photocatalysts for artificial photosynthesis and environmental remediation: are we a step closer to achieving sustainability?. *Chem. Rev.* <https://doi.org/10.1021/acs.chemrev.6b00075> (2016).
48. Du, A. *et al.* Hybrid graphene and graphitic carbon nitride nanocomposite: Gap opening, electron-hole puddle, interfacial charge transfer, and enhanced visible light response. *J. Am. Chem. Soc.* **134**, 4393–4397 (2012).
49. Rono, N., Kibet, J. K., Martincigh, B. S. & Nyamori, V. O. A review of the current status of graphitic carbon nitride. *Crit. Rev. Solid State Mater. Sci.* **46**, 189–217 (2021).
50. Ismael, M. & Wu, Y. A mini-review on the synthesis and structural modification of g-C₃N₄-based materials, and their applications in solar energy conversion and environmental remediation. *Sustain. Energy Fuels* **3**, 2907–2925 (2019).
51. Malik, R. & Tomer, V. K. State-of-the-art review of morphological advancements in graphitic carbon nitride (g-CN) for sustainable hydrogen production. *Renew. Sustain. Energy Rev.* **135**, 110235 (2021).
52. Nasir, M. S. *et al.* Recent development in graphitic carbon nitride based photocatalysis for hydrogen generation. *Appl. Catal. B Environ.* **257**, 117855 (2019).
53. Tang, S., Zhu, Y., Li, H., Xu, H. & Yuan, S. Two-dimensional carbon nitride-based composites for photocatalytic hydrogen evolution. *Int. J. Hydrogen Energy* **44**, 30935–30948 (2019).
54. Wang, Y., Liu, L., Ma, T., Zhang, Y. & Huang, H. 2D graphitic carbon nitride for energy conversion and storage. *Adv. Funct. Mater.* **31**, 1–36 (2021).
55. Li, X., Masters, A. F. & Maschmeyer, T. Polymeric carbon nitride for solar hydrogen production. *Chem. Commun.* **53**, 7438–7446 (2017).
56. Mao, N. Investigating the heterojunction between ZnO/Fe₂O₃ and g-C₃N₄ for an enhanced photocatalytic H₂ production under visible-light irradiation. *Sci. Rep.* **9**, 1–9 (2019).
57. Zhang, Z., Liu, K., Feng, Z., Bao, Y. & Dong, B. Hierarchical sheet-on-sheet ZnIn₂S₄/g-C₃N₄ Heterostructure with highly efficient Photocatalytic H₂ production based on Photoinduced interfacial charge transfer. *Sci. Rep.* **6**, 1–10 (2016).

58. Zhu, Q., Xu, Z., Qiu, B., Xing, M. & Zhang, J. Emerging cocatalysts on g-C₃N₄ for photocatalytic hydrogen evolution. *Small* **17**, 1–25 (2021).
59. Tan, M. *et al.* Engineering of g-C₃N₄-based photocatalysts to enhance hydrogen evolution. *Adv. Colloid Interface Sci.* **295**, 102488 (2021).
60. Stroyuk, O. *et al.* Tuning the surface plasmon resonance in gold nanocrystals with single layer carbon nitride. *RSC Adv.* **9**, 444–449 (2019).
61. Xu, J., Zhang, L., Shi, R. & Zhu, Y. Chemical exfoliation of graphitic carbon nitride for efficient heterogeneous photocatalysis. *J. Mater. Chem. A* **1**, 14766–14772 (2013).
62. Stroyuk, A. L., Shvalagin, V. V., Kotenko, I. E., Kuchmii, S. Y. & Plyusnin, V. F. Photochemical reduction of sulfur in the presence of ZnO nanoparticles in ethanol. *Theor. Exp. Chem.* **46**(4), 218–224 (2010).
63. Rong, X. *et al.* Fabrication of single-layer graphitic carbon nitride and coupled systems for the photocatalytic degradation of dyes under visible-light irradiation. *Eur. J. Inorg. Chem.* **2015**, 1359–1367 (2015).
64. Nouruzi, N. *et al.* Selective catalytic generation of hydrogen over covalent organic polymer supported Pd nanoparticles (COP-Pd). *Mol. Catal.* **493**, 111057 (2020).
65. Doustkhah, E. *et al.* Organosiloxane tunability in mesoporous organosilica and punctuated Pd nanoparticles growth; theory and experiment. *Microporous Mesoporous Mater.* **293**, 109832 (2020).
66. Nouruzi, N. *et al.* Photocatalytic hydrogen generation using colloidal covalent organic polymers decorated bimetallic Au-Pd nanoalloy (COPs/Pd-Au). *Mol. Catal.* **518**, 112058 (2022).
67. Doustkhah, E. *et al.* Templated synthesis of atomically-thin Ag nanocrystal catalysts in the interstitial space of a layered silicate. *Chem. Commun.* **54**, 4402–4405 (2018).
68. Nouruzi, N., Dinari, M., Gholipour, B., Afshari, M. & Rostamnia, S. In Situ Organized Pd and Au Nanoparticles in a Naphthalene-Based Imine-Linked Covalent Triazine Framework for Catalytic Suzuki Reactions and H₂ Generation from Formic Acid. *ACS Appl. Nano Mater.* (2022).
69. Ahadi, A. *et al.* Layer-wise titania growth within dimeric organic functional group viologen periodic mesoporous organosilica as efficient photocatalyst for oxidative formic acid decomposition. *ChemCatChem* **11**, 4803–4809 (2019).
70. Ma, T. Y., Dai, S., Jaroniec, M. & Qiao, S. Z. Graphitic carbon nitride nanosheet-carbon nanotube three-dimensional porous composites as high-performance oxygen evolution electrocatalysts. *Angew. Chemie - Int. Ed.* **53**, 7281–7285 (2014).
71. Zhao, H. *et al.* Fabrication of atomic single layer graphitic-C₃N₄ and its high performance of photocatalytic disinfection under visible light irradiation. *Appl. Catal. B Environ.* **152–153**, 46–50 (2014).
72. Mohan, S. *et al.* Dual probes of Ag/Pd bimetallic NPs facilely synthesized by green process using Catharanthus leaf extract on textile dye removal and free radical capability. *Appl. Nanosci.* **11**, 1565–1574 (2021).
73. Eken Korkut, S., Küçükkeçeci, H. & Metin, Ö. Mesoporous graphitic carbon nitride/black phosphorus/AgPd alloy nanoparticles ternary nanocomposite: A highly efficient catalyst for the methanolysis of ammonia borane. *ACS Appl. Mater. Interfaces* **12**, 8130–8139 (2020).
74. Ma, J. *et al.* The preparation and photocatalytic activity of Ag-Pd/g-C₃N₄ for the coupling reaction between benzyl alcohol and aniline. *Mol. Catal.* **476**, 110533 (2019).
75. Fang, J., Fan, H., Li, M. & Long, C. Nitrogen self-doped graphitic carbon nitride as efficient visible light photocatalyst for hydrogen evolution. *J. Mater. Chem. A* **3**, 13819–13826 (2015).
76. Wang, P., Guan, Z., Li, Q. & Yang, J. Efficient visible-light-driven photocatalytic hydrogen production from water by using Eosin Y-sensitized novel g-C₃N₄/Pt/GO composites. *J. Mater. Sci.* **53**, 774–786 (2018).
77. Qiao, F., Wang, J., Ai, S. & Li, L. As a new peroxidase mimetics: The synthesis of selenium doped graphitic carbon nitride nanosheets and applications on colorimetric detection of H₂O₂ and xanthine. *Sensors Actuators, B Chem.* **216**, 418–427 (2015).
78. Fu, G. T., Liu, C., Zhang, Q., Chen, Y. & Tang, Y. W. Polyhedral palladium-silver alloy nanocrystals as highly active and stable electrocatalysts for the formic acid oxidation reaction. *Sci. Rep.* **5**, 1–9 (2015).
79. Khan, S. *et al.* A semiconducting copper(II) coordination polymer with (4,4) square grid topology: Synthesis, characterization, and application in the formation of a photoswitch. *Cryst. Growth Des.* **18**, 651–659 (2018).
80. Gu, X., Lu, Z. H., Jiang, H. L., Akita, T. & Xu, Q. Synergistic catalysis of metal-organic framework-immobilized au-pd nanoparticles in dehydrogenation of formic acid for chemical hydrogen storage. *J. Am. Chem. Soc.* **133**, 11822–11825 (2011).

Author contributions

B.G wrote the main manuscript text and did perform the experimental tests. S.R, and A.Z, are supervisors and reviewed the manuscript. M.S reviewed the manuscript and did some analysis.

Competing interests

The authors declare no competing interests.

Additional information

Supplementary Information The online version contains supplementary material available at <https://doi.org/10.1038/s41598-022-17238-4>.

Correspondence and requests for materials should be addressed to A.Z. or S.R.

Reprints and permissions information is available at www.nature.com/reprints.

Publisher's note Springer Nature remains neutral with regard to jurisdictional claims in published maps and institutional affiliations.



Open Access This article is licensed under a Creative Commons Attribution 4.0 International License, which permits use, sharing, adaptation, distribution and reproduction in any medium or format, as long as you give appropriate credit to the original author(s) and the source, provide a link to the Creative Commons licence, and indicate if changes were made. The images or other third party material in this article are included in the article's Creative Commons licence, unless indicated otherwise in a credit line to the material. If material is not included in the article's Creative Commons licence and your intended use is not permitted by statutory regulation or exceeds the permitted use, you will need to obtain permission directly from the copyright holder. To view a copy of this licence, visit <http://creativecommons.org/licenses/by/4.0/>.

© The Author(s) 2022